Acta Materialia 256 (2023) 119111

Contents lists available at ScienceDirect

Acta Materialia

journal homepage: www.elsevier.com/locate/actamat

High-coercivity $SmFe_{12}$-based anisotropic sintered magnets by Cu addition

A.K. Srinithi [a,b], Xin Tang [a,c,*], H. Sepehri-Amin [a,b], J. Zhang [a], T. Ohkubo [a], K. Hono [a,b]

[a] National Institute for Materials Science, Tsukuba 305-0047, Japan
[b] Graduate School of Science and Technology, University of Tsukuba, Tsukuba 305-8577, Japan
[c] International Center for Young Scientist, National Institute for Materials Science, Tsukuba 305-0047, Japan

ARTICLE INFO

Keywords:
Hard magnets
$SmFe_{12}$ sintered magnets
Coercivity: Microstructure

ABSTRACT

We achieved a record-high coercivity of 1.40 T in a $SmFe_{12}$-based $ThMn_{12}$-type anisotropic sintered magnet. This magnet was prepared by sintering jet-milled powder made from strip-cast alloys with a nominal composition of $Sm_8Fe_{73.5}Ti_8V_8Al_2Cu_{0.5}$, using the conventional process for anisotropic sintered magnet production. Detailed microstructural investigations conducted using scanning electron microscopy and transmission electron microscopy revealed that the formation of Fe-lean intergranular phases (with < 20 at.% of Fe) surrounding the fine $SmFe_{12}$ phase grains resulted in the high coercivity. Nanobeam electron diffraction patterns showed that these Fe-lean intergranular phases (IGPs) exhibiting excellent wettability in this magnet are mainly composed of two phases: a hexagonal close-packed Mg-type Sm-based phase and a primitive cubic CsCl-type SmCu-based phase, which co-exist in the same intergranular region. Such Fe-lean IGPs minimize the intergranular exchange coupling in the $SmFe_{12}$ main phase, which contributes to the high coercivity, as revealed by magneto-optical Kerr effect microscopy. Overall, this study provides detailed microstructure-coercivity correlations and insights for the future development of high-performance $SmFe_{12}$-based sintered magnets.

1. Introduction

An increasing demand for permanent magnets (PMs) is driven by the global transition in favor of green energy technologies, wherein the PM-based motors and generators play major roles in efficient energy conversions [1–4]. Currently, the (Dy,Nd)–Fe–B magnets are mainly used for these applications, but the high cost of the rare earth elements, Nd and Dy, has led to accelerated research towards finding an alternative cost-effective PM [5,6]. The rare-earth-lean $SmFe_{12}$-based hard-ferromagnetic compounds with a strong uniaxial magneto-crystalline anisotropy have been intensively studied as candidates for permanent magnets [7–9]. These compounds have the $ThMn_{12}$-type structure, which needs to be stabilized by the substitution of elements such as Ti, V, or their combinations. Owing to its low material cost and promising intrinsic magnetic properties, the $SmFe_{12}$--based compound has the potential for a better performance-to-cost ratio and hence is considered as a next-generation permanent magnet candidate [10,11]. To make this practical, extensive research is being carried out to improve its extrinsic magnetic properties, mainly its coercivity (H_c).

The coercivity is governed by various microstructural features, such as grain size, grain morphology, presence of secondary phases, type of intergranular phase and its chemical composition (magnetism), and interfacial defects [12,13]. For instance, the presence of secondary ferromagnetic phases can deteriorate the coercivity; the formation of a non-ferromagnetic intergranular phase (IGP) can improve the coercivity owing to weakened intergranular exchange-coupling in the main phase. Several fundamental studies have been conducted on coercivity enhancement of the $Sm(Fe,Ti)_{12}$-based compound [14–22]. Gabay *et al.* reported the highest coercivity of 1.26 T in monocrystalline $Sm(Fe,Ti)_{12}$-based powder made by the reduction–diffusion process [14]. However, many factors hinder the realization of high coercivity values in bulk $Sm(Fe,Ti)_{12}$-based alloys. The major bottlenecks include the inability to eliminate secondary soft-ferromagnetic phases and to form Fe-lean IGPs surrounding the hard-ferromagnetic $SmFe_{12}$ grains [15–22]. Recently, a study comparing TiV-stabilized $SmFe_{10}TiV$ (μ_0H_c = 1.1 T) and Ti-stabilized $SmFe_{11}Ti$ (μ_0H_c = 0.5 T) melt-spun ribbons, demonstrated that the existence of Fe-lean IGPs surrounding the $SmFe_{12}$ grains is the key reason for the higher coercivity of V-doped ribbons [21]. Otsuka *et al.* carried out a similar comparative study on sintered magnets, and found that the V-stabilized $Sm(Fe,V)_{12}$ alloy had a high coercivity (0.8 T) owing to the formation of Fe-lean IGPs, whereas the

* Corresponding author.
E-mail address: Tang.Xin@nims.go.jp (X. Tang).

https://doi.org/10.1016/j.actamat.2023.119111
Received 2 January 2023; Received in revised form 22 June 2023; Accepted 25 June 2023
Available online 26 June 2023

Ti-stabilized $Sm(Fe,Ti)_{12}$ alloy did not have IGPs but had secondary soft-ferromagnetic phases, and thus a low coercivity (~0.01 T) [22]. These reports show that V substitution for Fe is crucial in terms of avoiding the undesired secondary phases while maintaining the microstructure favorable for high coercivity. However, the reported coercivity for the $SmFe_{12}$-based anisotropic sintered magnets is limited to 0.8–1.0 T, which is only ~10% of their anisotropy field and is insufficient for practical applications [22,23]. Hence, further work on tuning the microstructure of the $SmFe_{12}$-based magnets needs to be conducted to fully utilize its strong anisotropy field and improve the coercivity.

The limited coercivity in previously reported anisotropic sintered magnets possibly originate from coarse $SmFe_{12}$-based grains and the high Fe content in the IGPs. The average grain size in these sintered magnets was mostly around 9–10 μm [22,24]. Hence, grain refinement approaching the single domain size (0.6 to 0.75 μm) [23] is expected to improve the coercivity of the $SmFe_{12}$-based magnets. Note that the previously reported $SmFe_{12}$-based anisotropic magnets were prepared using optimally annealed as-cast ingots as the starting material [22–24]. It is known from the conventional metallurgical process for sintered Nd–Fe–B magnets, that the grain size of the final product can be refined by the use of strip-cast alloys as the starting material for the powder preparation [25]. A similar processing method needs to be investigated for the $SmFe_{12}$ sintered magnets. Furthermore, the Fe concentration in IGPs has been reported to be around 50 at.% in the previous studies on $SmFe_{12}$-based sintered magnets [22,23]. For example, in the $SmFe_{10}V_2$ sintered magnets by Otsuka *et al.*, the $SmFe_{12}$ grains were separated by 2 nm thick Sm–Fe-based IGPs in several regions, and the Fe content in these IGPs was between 40 to 50 at.% [22]. Zhang *et al.* reported a higher coercivity of 1 T in $Sm_8Fe_{73.5}Ti_8V_8Al_2Ga_{0.5}$ magnets, where the IGPs had 45–55 at.% of Fe [23]. A reduction of the Fe content in the IGP can lead to its lower magnetization, and thus weaker intergranular exchange coupling, leading to higher coercivities in $SmFe_{12}$-based sintered magnets. Recently, Schönhöbel *et al.* reported an improvement in the coercivity from 0.88 to 0.96 T by doping Cu in nanocrystalline Sm–Fe–V-based isotropic magnets [26]. Ogawa *et al.* also reported that grain boundary infiltration of Cu in $SmFe_{12}$ thin films resulted in coercivity enhancement [27]. Similar compositional modification can help in improving the coercivity of the $SmFe_{12}$-based anisotropic sintered magnets as well.

In this study, by modifying the processing method and microalloying with Cu, Fe-lean IGPs enveloping the main phase grains are obtained. As a result, a record-high coercivity of 1.4 T was achieved in the $SmFe_{12}$-based anisotropic sintered magnets. Detailed investigations were performed to gain understanding on how the overall microstructure, and the nature of the intergranular phases influence the coercivity.

2. Experimental

Ingots with the composition of $Sm_8Fe_{74}Ti_8V_8Al_2$ (denoted as Cu0) and $Sm_8Fe_{73.5}Ti_8V_8Al_2Cu_{0.5}$ in at.% (denoted as Cu0.5) were prepared by melting and casting in an induction furnace, with appropriate amounts of excess Sm added to compensate for the evaporation. Unlike in the previous reports [22–24], the strip-casting technique was employed in this study to produce alloys for powder preparation. The as-cast ingots were strip-cast into flakes using a Cu wheel with a quenching-surface speed of 1–2 m/s, after which the flakes were annealed at 1273 K for 9 h under Ar atmosphere to facilitate phase formation. Hydrogen decrepitation was carried out such that the strip-cast flakes could be easily crushed into powder, followed by jet milling with N_2 gas at 1.0 MPa in an Ar-filled glove box. The jet-milled powders were oriented using a pulse magnetizer, pressed into a green compact, and sintered at 1373 K for 2 h. These sintered magnets (which were made with the strip-cast flakes as the starting material) are referred to as the Cu0 and Cu0.5 magnets based on their compositions. To elucidate the effect of using strip-cast flakes as the starting material, a sintered magnet was also produced using annealed ingots as the starting material for comparison, which is referred to as the Cu0.5-I magnet. The density values of the sintered magnets were found to be ~7.3 g/cm^3.

Magnetic hysteresis (*M–H*) loops were measured using a 14 T physical property measurement system with a vibrating sample magnetometer setup (VSM). The oven-module connected to the VSM was used to measure the temperature-dependent coercivity. A Carl Zeiss Cross-Beam 550 scanning electron microscope (SEM) equipped with an in-lens detector was used to observe the overall microstructure. Detailed analysis of the crystal structure and the composition of the constituent phases was conducted using an FEI Titan G2 80-200 transmission electron microscope (TEM) with a probe aberration corrector coupled with an EDS detector. The TEM specimen was prepared by the lift-out method using an FEI Helios G4-UX focused ion beam system. A magneto-optical Kerr effect (MOKE) microscope, equipped with 1.2 T electromagnets, was used to observe the magnetization reversal dynamics. Powder X-ray diffraction patterns for phase identification were obtained using a Rigaku MiniFlex X-ray diffractometer with Cr–Kα radiation.

3. Results

3.1. Magnetic properties

Fig. 1(a) shows the magnetic hysteresis (*M–H*) along the easy axis of the anisotropic Cu0 and Cu0.5 sintered magnets, which were produced using strip-cast flakes as the starting material. The remanent magnetization and coercivity values are 0.61 and 0.95 T for the Cu0 magnet, and 0.6 T and 1.4 T for the Cu0.5 magnet; the $(BH)_{max}$ values were found to be 57.3 and 67.8 kJ/m^{-3}, respectively. The coercivity of 1.4 T obtained for the Cu0.5 magnet is the highest reported so far for the $SmFe_{12}$-based magnets. For reference, the *M-H* loops and corresponding XRD profiles at the various stages of processing is presented in the Supplementary Figure S1 for the Cu0.5 magnet.

The temperature dependence of coercivity for the Cu0 and Cu0.5 magnets compared to a high-coercivity Nd–Fe–B sintered magnet [28,29] is shown in Fig. 1(b). Here, the Nd-Fe-B sintered magnet with a high coercivity ($\mu_0 H_c$ =1.8 T, H_c/H_A = 0.26) is selected for comparison. The temperature coefficient of coercivity, $\beta = [H_c(T) - H_c(RT)]/[H_c(RT) *\Delta T]$, is –0.57% K^{-1} for the Cu0 magnet in the temperature range 300 K to 420 K, which is significantly improved to –0.45% K^{-1} (in the Cu0.5 magnet) after microalloying with Cu. This β value is larger than that (–0.55% K^{-1}) of the high-coercivity Nd-Fe-B sintered magnet, showing that the coercivity of the Cu0.5 $SmFe_{12}$-based magnet is more thermally stable, while that of the Cu0 magnet is not. Therefore, the Cu0.5 $SmFe_{12}$-based magnet exhibits a higher coercivity above 380 K compared to the Nd-Fe-B sintered magnet, regardless of its lower coercivity at room temperature. At the typical operating temperature of 423 K, the coercivity of the Cu0.5 magnet is 0.63 T, which is higher than that of the Nd–Fe–B magnet (0.57 T) [29]. Moreover, there is no significant variation in β with the temperature for the Cu0.5 magnet, unlike Cu0, where it varies from –0.63 to –0.49 % K^{-1}, as presented in Fig. 1(c). The relatively stable β against temperature in the Cu0.5 magnet might indicate the lower magnetization of the intergranular phases than that in the Cu0 magnet according to Ref. [30]. By treating the temperature dependence of the coercivity with that of the intrinsic properties, anisotropy field (H_A) and saturation magnetization (M_s) (adopted from Ref. [23]), according to H_c (T) = αH_A(T) – $N_{eff} M_s$(T) [31] as shown in Fig. 1(d), the microstructural parameters, α and N_{eff} were obtained. The enhanced α and reduced N_{eff} of the Cu0.5 magnet (α = 0.20; N_{eff} = 0.68) compared to the Cu0 magnet (α = 0.17; N_{eff} = 0.89). In addition, we found that the Cu0.5-I magnet made from ingots as the starting material, has a much lower coercivity (0.85 T) than the Cu0.5 magnet, although the composition was the same, indicating that the processing route is also critical. To understand the reason for the improved coercivity in the Cu0.5 magnet, a detailed microstructural analysis using the combination of SEM and TEM was conducted.

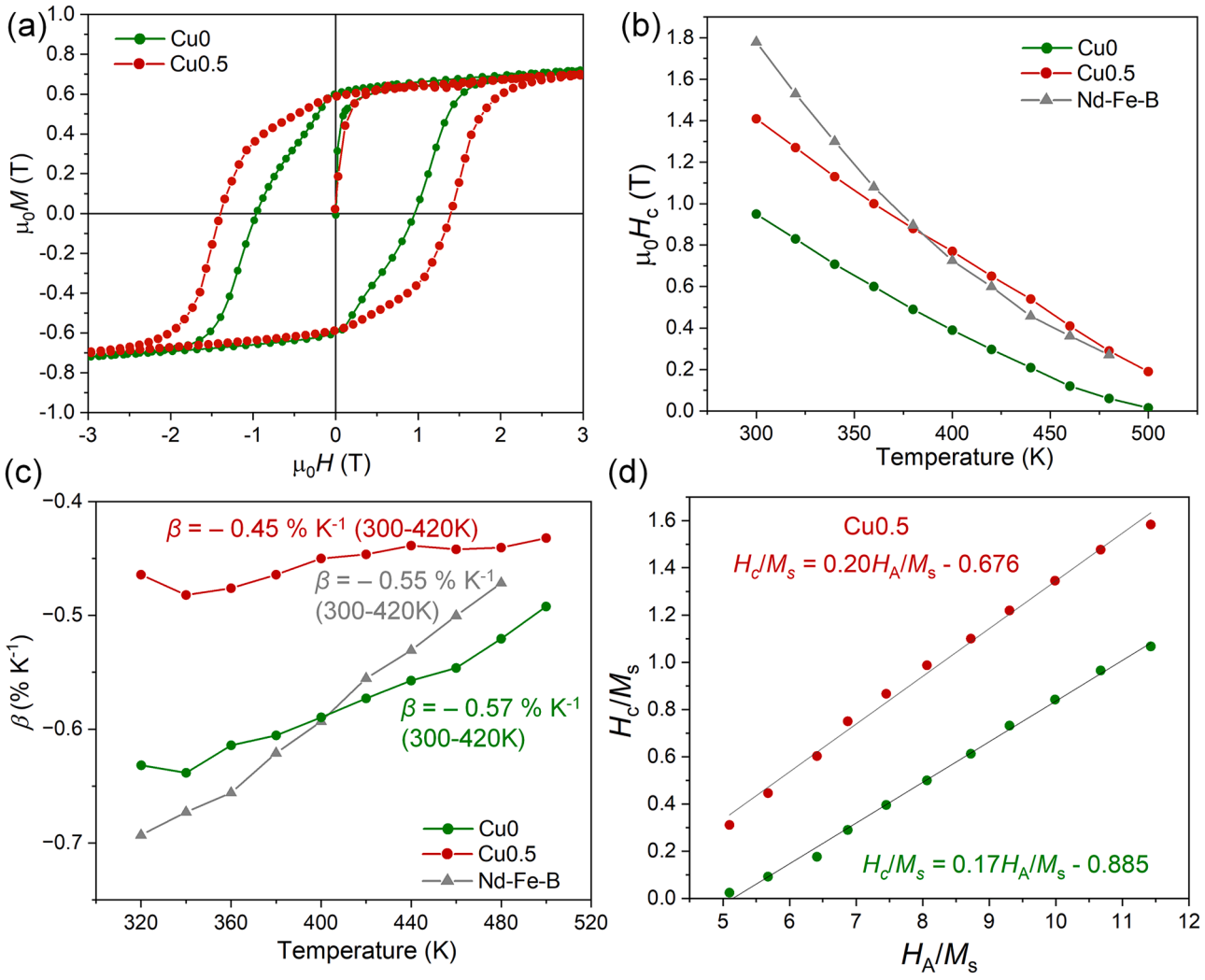

Fig. 1. (a) *M–H* hysteresis loops of the Cu0 and Cu0.5 sintered magnets measured along the easy axis. (b) Temperature-dependent coercivity values and (c) temperature coefficient of coercivity (β) of the Cu0, Cu0.5 and Nd–Fe–B [28] sintered magnets. (d) Linear fitting of H_c/M_s vs. H_A/M_s values to obtain the Kronmüller equation for the Cu0 and Cu0.5 magnets.

3.2. Overall microstructure

Fig. 2 shows the SEM micrographs obtained from the in-lens secondary electron (IL-SE) and back scattered electron (BSE) detectors, where the various phases present in the Cu0, Cu0.5 and Cu0.5-I sintered magnets can be differentiated based on the image contrast. The main phase is the $SmFe_{12}$-based phase and its mean grain size (d_m) is ~2.6 μm ± 1.0 μm for the Cu0 magnet and ~4.2 ± 1.2 μm for the Cu0.5 magnet, shown in detail in Fig. S2. Compared to the previous reports on $SmFe_{12}$-based sintered magnets, we achieved smaller grain size, approaching the single domain size (~0.6–0.75 μm) [23]. The overall grain size achieved may have been influenced by the particle size (~2 μm) of the as-jet milled powder (as detailed in Fig. S3), and the presence of secondary phases.

The phases showing bright contrast in the BSE image of Fig. 2(a) correspond to Sm enriched phases such as Sm-based and Sm–O-based phases; in addition to these phases, Sm–Cu-based phase can be seen in the Cu0.5 magnet (Fig. 2(b)). The Sm-based phase has the brightest contrast in both the IL-SE and BSE images. The Sm–O-based phase has almost the same contrast as the Sm-based phase in the BSE image, while it appears to be darker in the IL-SE image. In the Cu0.5 magnet, the Sm–Cu-based phase can be differentiated due to its relatively darker contrast with respect to the Sm-based phase in the BSE image. The phases having dark contrast with respect to the $SmFe_{12}$-based main phase correspond to the Ti-rich phases (Fe_2Ti and Ti). The volume fraction of the constituent phases was found by Rietveld refinement of the XRD profile and presented in the Fig. S4 for the Cu0 and Cu0.5 magnets. In the Cu0.5 magnet, the triple junction phases that can be related to coercivity enhancement, the Sm-based and SmCu-based phases, are 4.7 % and 2.6 %, respectively, in contrast to the Cu0 magnet which has 6.3% of only the Sm-based phase.

Of particular interest is that the IGPs with bright contrast along the grain boundaries is visible in both the IL-SE and BSE images in the Cu0.5 magnet (Fig. 2(b)), indicative of the strong partitioning of the heavier element, i.e., Sm in the IGPs. In contrast, the IGPs are not distinctly visible and it is very rare to find bright contrast features along the grain boundaries in the Cu0 magnet. The above microstructure comparison suggests that the better wettability of Sm-rich IGPs surrounding the matrix grains achieved in the Cu0.5 magnet could be attributed to the microalloying with Cu. On the other hand, the Cu0.5-I magnet shown in Fig. 2(c) does not have clearly visible Sm-rich IGPs compared to the Cu0.5 magnet. Therefore, the good coverage of the Sm-rich IGPs in the Cu0.5 magnet is not only attributed to its composition, but also to the process route followed, which used strip-cast flakes as the starting material. The reason for the improved Sm-rich IGP coverage in the Cu0.5 magnet than that in the Cu0.5-I magnet, could be attributed to a better

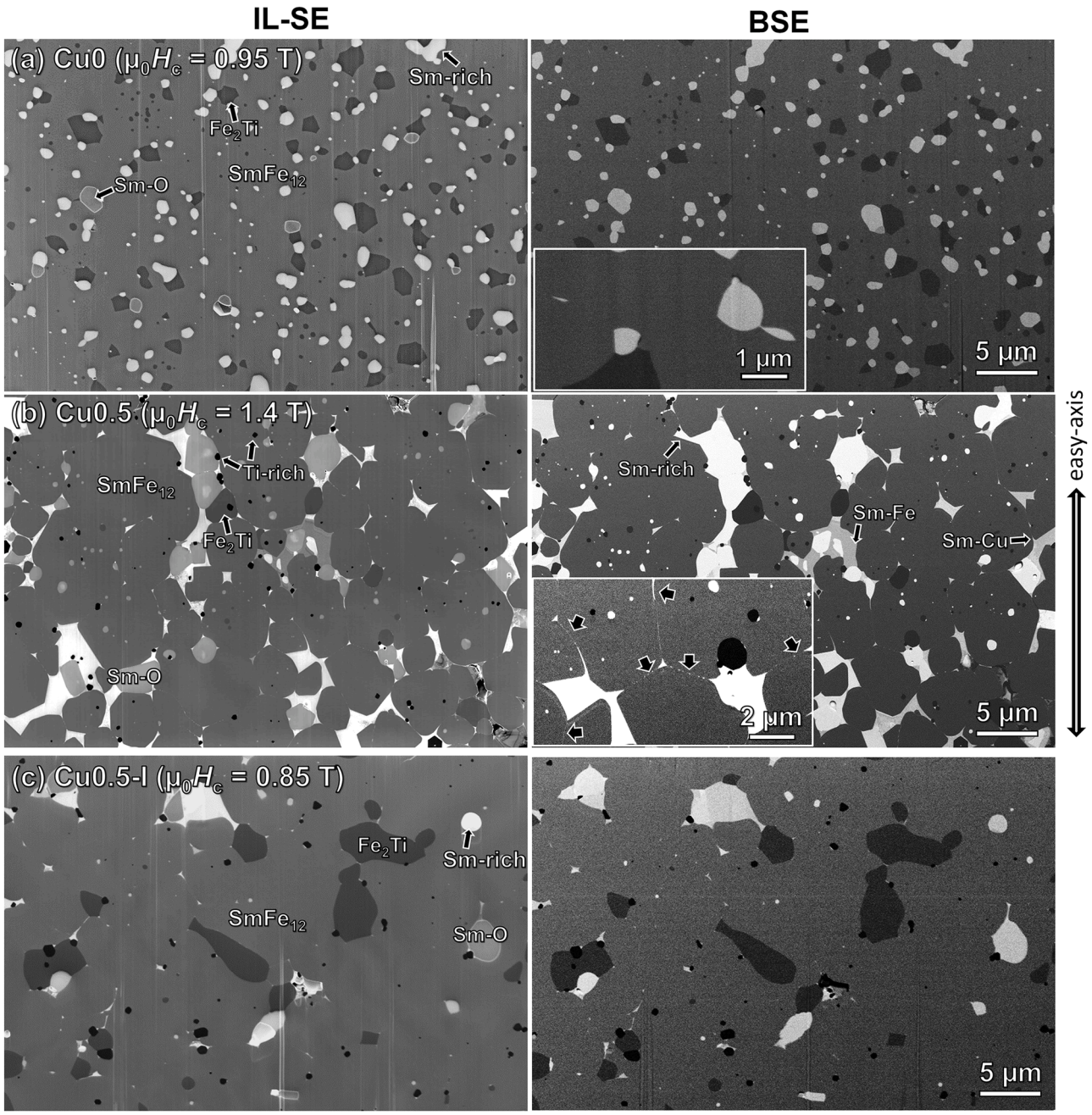

Fig. 2. In-lens secondary electron (IL-SE) and back-scattered electron (BSE) SEM images of the (a) Cu0 (b) Cu0.5 and (c) Cu0.5-I sintered magnets.

homogeneity and distribution of the Sm-enriched phases in the strip-cast flakes than that in the ingots (Supplementary Fig. S3). Overall, the SEM observation indicates that the enhanced coercivity of the Cu0.5 magnet originated by the formation of Sm-rich IGPs with a good coverage, which is obtained via Cu-addition and the use of strip-cast flakes as the starting material. As the intergranular chemistry can be a crucial contributor to the coercivity, detailed compositional analysis of IGP phases was performed.

3.3. Nanochemistry of the intergranular phases

Fig. 3(a) shows a high-resolution HAADF-STEM image presenting a *c*-plane intergranular phase for the Cu0 magnet. The IGP is ~3 nm thick with the composition of $\sim Sm_{19.5}Fe_{55}Al_{12.5}Ti_5V_8$ (at.%), as shown in the concentration profiles. In the Cu0.5 magnet (Fig. 3(b)), the IGP has a composition of $\sim Sm_{64.6}Fe_{14.2}Al_{9.8}Ti_{3.7}V_{3.9}Cu_{3.8}$ (at.%). The Fe content in the IGP is around ~14 at.%, which is significantly lower compared to that of the Cu0 magnet (55 at.%), as well as the previously-reported $SmFe_{12}$-based sintered magnets, where the Fe content was around ~45–55 at.% [22,23]. Although the error from these nanometer-scale analysis is unavoidable, the relative change of the Fe concentration in the IGP between the Cu0 and Cu0.5 magnets is considerably large. This reduction of the Fe content in the IGP weakens the intergranular exchange-coupling and contributes to the increase in coercivity. It is noteworthy that close to the interfaces between the IGP region and the $SmFe_{12}$ phase, enrichment of Cu is observed. Moreover, it was found that the Sm-rich intergranular phases are less pronounced in the SEM images when the c-axis is out-of-plane, compared to the case in which the easy-axis is in-plane (Fig. S5), wherein the Sm-rich IGPs are not found for some regions in the former. Fig. 3(c) shows a high-resolution STEM–HAADF image of an *ab*-plane IGP of the Cu0.5 magnet. The composition (having ~18 at.% Fe) and thickness are similar to those of

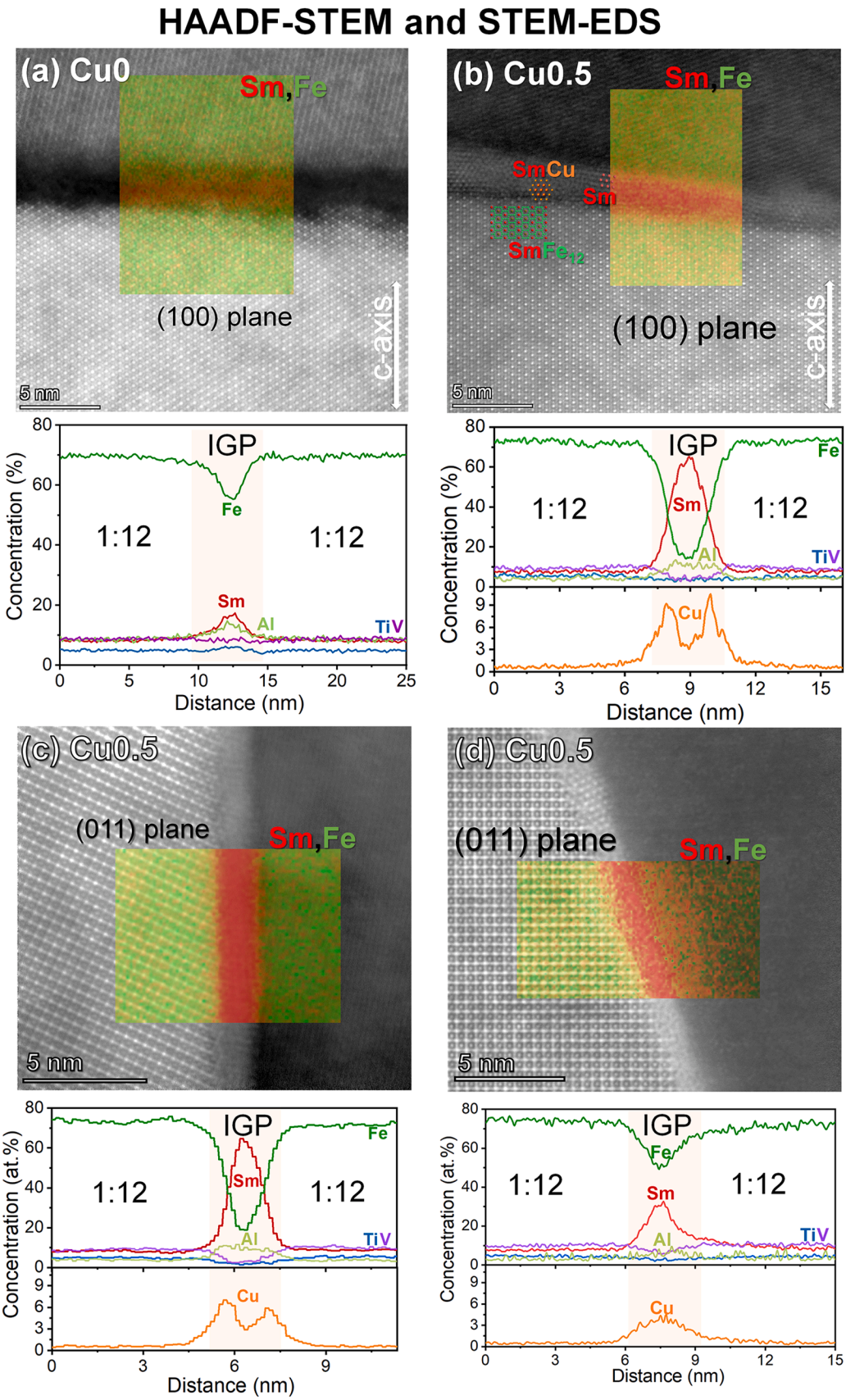

Fig. 3. High-resolution HAADF-STEM images super-imposed with EDS maps, and corresponding elemental concentration profiles for *c*-plane IGPs of the (a) Cu0 and (b) Cu0.5 magnets, and for (c), (d) *ab*-plane IGPs of the Cu0.5 magnet.

the *c*-plane IGP, and the Cu-enrichment near the interfaces between the $SmFe_{12}$ phase and the IGP region can also be observed. Another case of the *ab*-plane intergranular phase is shown in Fig. 3(d), where the Sm concentration in the IGP is only about 32 at.%. Correspondingly, there is a large amount of Fe (50.4 at.%) in this IGP. There is no Cu-enrichment in the $SmFe_{12}$/IGP interface in this case, in contrast to the other IGPs observed. This denotes that Cu plays a vital role in suppressing the Fe content of the IGP, which in turn results in high coercivity values. In addition, it should be noted that the Cu content within the $SmFe_{12}$ grains is negligible, showing that the role of Cu is only in the tuning of IGP magnetism, while not affecting the magnetization of the main phase. Hence, the addition of Cu in the $SmFe_{12}$-based sintered magnets is highly desirable for optimizing the microstructure to achieve a high coercivity. As the Cu0.5 magnet has promising grain boundary chemistry leading to the high coercivity, we performed detailed analysis to find the crystal structure of the triple junction phases and the IGPs in this magnet.

3.4. Crystal structures of triple junction and intergranular phases (Cu0.5 magnet)

Fig. 4(a) and (c) show the STEM–EDS maps, and Fig. 4(b) and (d) show the nano-beam electron diffraction (NBED) patterns from the constituent phases of the Cu0.5 magnet. The Sm-rich triple-junction phases with bright contrast in the BSE-SEM images (Fig. 2(b)) are marked in the STEM–EDS maps, and their compositions are presented in Table 1. In Fig. 4(a), Region II, which shows the brightest contrast in both the IL-SE and BSE-SEM images (Fig. 2(b)), has the composition, $Sm_{83.6}Fe_{8.7}Al_{4.4}Cu_{1.2}V_{1.5}Ti_{0.6}$ (at.%), and its NBED patterns reveal the hexagonal close-packed Mg-type crystal structure (P63/mmc). The low Fe content (8.57 at.%) of this phase is indicative of its non-ferromagnetic nature. Regions III and IV correspond to the Sm–O and Sm–Cu regions marked in the SEM images, respectively (Fig. 2(b)). The region III has the SmO phase with the face-centered cubic NaCl-type structure. The composition of the Sm–Cu phase in the triple junction (Region IV) is determined to be $Sm_{52.1}Cu_{36.1}Fe_{5.3}Al_{5.5}V_{0.7}Ti_{0.3}$, and further NBED patterns reveal the primitive cubic SmCu-based phase with the CsCl-type structure ($Fm\bar{3}m$). Note that this phase also has a very small amount of Fe (~ 5.2 at.%) and is considered to be non-ferromagnetic. A thick Sm–Cu-based intergranular phase (IV-IGP) isolating the main phase grains can be seen extending from the SmCu triple junction (IV), which indicates its good wettability. This IV-IGP was also found to have the

Table 1
Compositions (at.%) of Sm-rich triple junction phases obtained from STEM–EDS for the Cu0.5 magnet.

Region	STEM-EDS Composition (at.%)	Phase
I	$Sm_{9.1}Fe_{74.2}Ti_{6.0}V_{8.9}Al_{1.5}Cu_{0.3}$	$ThMn_{12}$-type $SmFe_{12}$
II	$Sm_{83.6}Fe_{8.7}Al_{4.4}Cu_{1.2}V_{1.5}Ti_{0.6}$	HCP Mg-type Sm
III	$Sm_{48.4}O_{45.5}Fe_{3.8}Al_{2.3}$	FCC NaCl-type SmO
IV	$Sm_{52.1}Cu_{36.1}Fe_{5.3}Al_{5.5}V_{0.7}Ti_{0.3}$	PC CsCl-type SmCu

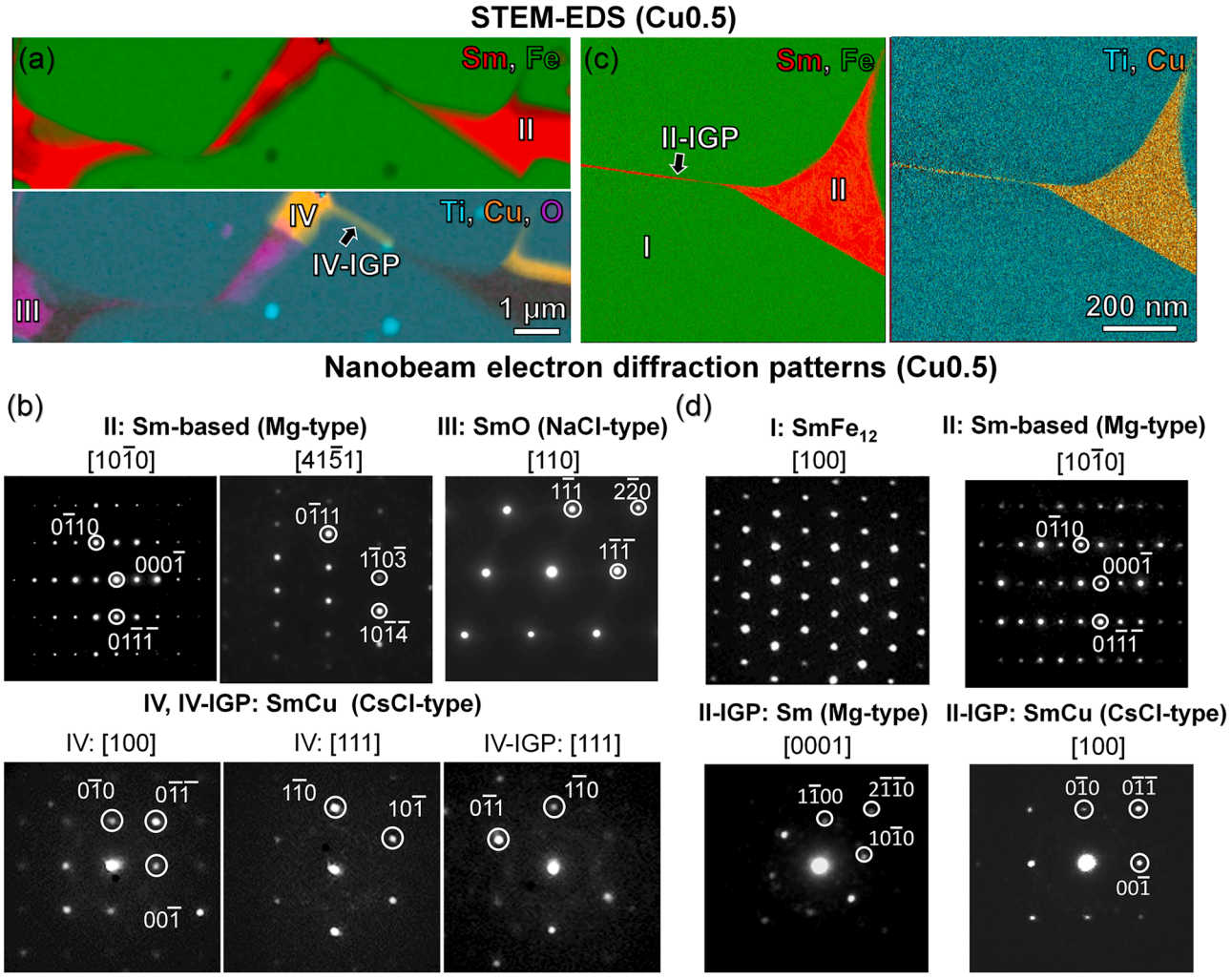

Fig. 4. (a), (c) STEM–EDS maps and (b), (d) respective sets of nano-beam electron diffraction patterns obtained from the different regions in the maps for the Cu0.5 magnet.

CsCl-type phase, the same as the SmCu triple junction phase, as shown in Fig. 4(b) (IV-IGP). Fig. 4(c) shows a case where the Mg-type Sm-based triple junction (Region II) has infiltrated into the nearby grain boundary, forming an intergranular phase (II-IGP). Interestingly, two different crystal structures were resolved by NBED within the II-IGP region: one is the Mg-type Sm-based phase, the same as the triple junction, the other being the CsCl-type SmCu-based phase (as shown in Fig. 4(d)). This observation indicates the existence of the (Sm+SmCu)-based low-melting eutectic around the $SmFe_{12}$ grains, which could be the reason for the good wettability of Fe-lean IGP network in the high-coercivity Cu0.5 magnet.

3.5. Magnetization reversal process

The above results showed that the high coercivity is mainly attributed to the formation of Fe-lean intergranular phases surrounding the $SmFe_{12}$ grains. Here, we investigate how the different Fe concentration in the IGPs can affect the magnetization reversal process using a magneto-optical Kerr effect (MOKE) microscope as shown in Fig. 5. The magnets are shown with its *c*-axis in-plane. Initially, they were saturated with an external magnetic field, and then the field was applied in the opposite direction. In most cases for both the Cu0 and Cu0.5 magnets, the nucleation of reversed domains (dark contrast) occurred near the secondary phases, due to the large stray field at these sites. In the Cu0 magnet (Fig. 5(a)), the nucleation of reverse domains can be seen in several regions for the applied field (H_{ex}) of -0.5 T. As H_{ex} slightly decreases to -0.7 T, the size of the reverse domains grows rapidly indicating a weak pinning force against reversed domain wall propagation. This is a result of the exchange-coupling of grains, through a relatively Fe-rich IGP as seen in Fig. 3(a). Only in a few regions, the restriction of the domain wall motion is seen (marked by arrows). As the field is further reduced to -0.9 T, the reversed domain propagates through almost all of the observed region. In contrast, in the Cu0.5 magnet (Fig. 5 (b)), nucleation and slight growth of reversed domain can be observed with a decrease of field from -0.4 T to -0.6 T. With further reduction of the external field to -1.1 T, strong pinning force can be clearly seen as the propagation of several reversed domains is restricted (marked by arrows). As a result, the size of the reversed domains is smaller than those in the Cu0 magnet. After the external field is reduced to -1.2 T, the reversed domains penetrate only into a few of the neighboring grains.

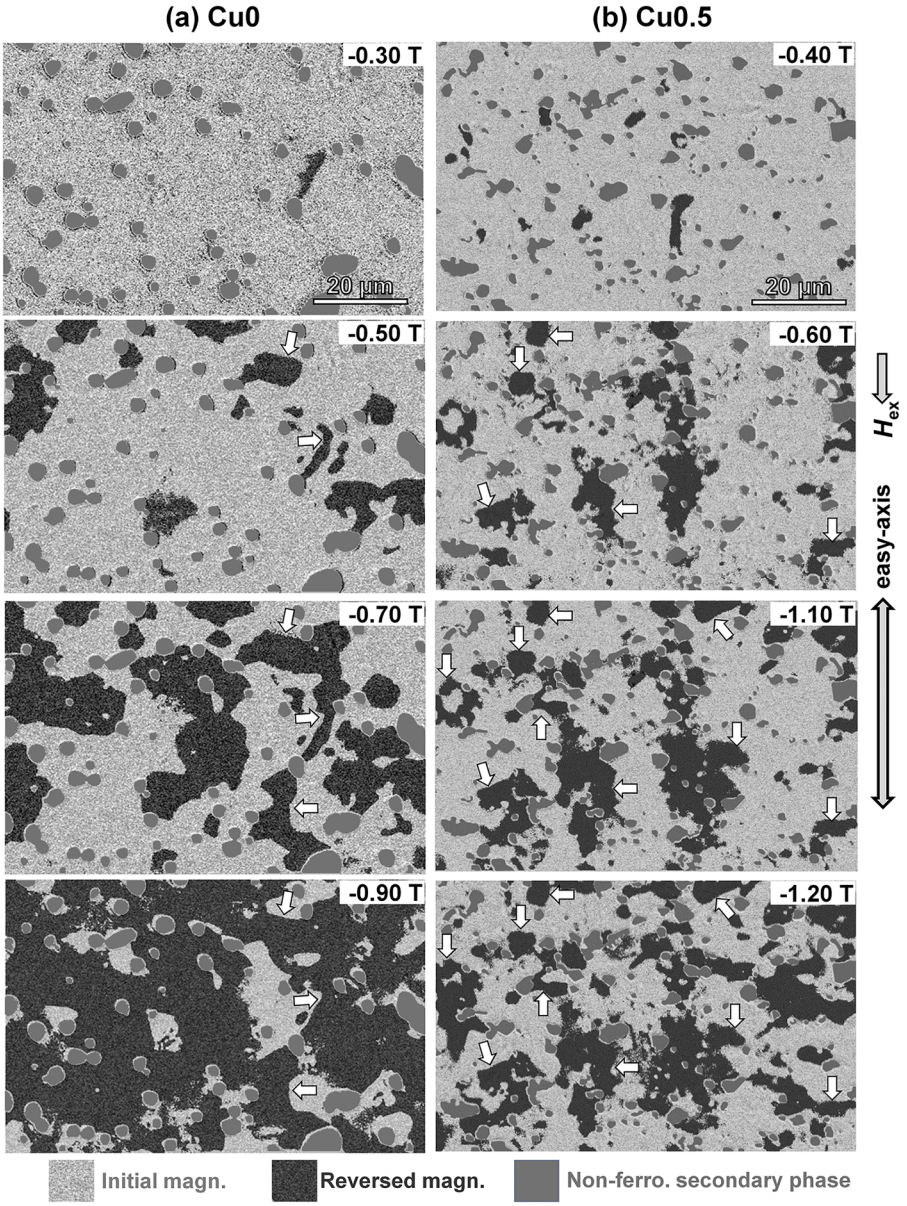

Fig. 5. Magneto-optical Kerr effect microscopy images of Cu0 and Cu0.5 magnets under different external magnetic field.

This indicates that the Cu0.5 magnet is more resistant to the demagnetizing field owing to the reduced Fe concentration in the IGPs, thus resulting in the high coercivity.

4. Discussion

In this work, we reported a record-high coercivity of 1.40 T in an anisotropic sintered Cu-containing $SmFe_{12}$-based magnet (Cu0.5) produced using strip-cast flakes as the starting material. The average grain size of the Cu0.5 magnet is ~4.2 μm, larger than that (~2.6 μm) of the Cu0 magnet; nevertheless, the coercivity of the Cu0.5 magnet (1.4 T) is higher than that (0.95 T) of Cu0 magnet. This indicates that the chemical composition of the intergranular phase could play a crucial role in the coercivity enhancement in this case. From the nano-chemical analysis (Fig. 3), it was found that the Fe content (< 20 at.%) of the IGPs in the Cu0.5 magnet was lower compared to that (~55 at.%) of the Cu0 magnet. The Fe-lean IGPs in the Cu0.5 magnet are represented by the Sm-based Mg-type and SmCu-based CsCl-type structures, co-existing within the intergranular regions (Fig. 4(d)). Note that a good connectivity of the IGP network based on these phases can be obtained provided that the magnet is prepared from strip-cast flakes as the starting material, as it ensures the desired uniform distribution of the Sm-rich triple junctions.

Based on the overall decrease of the Fe content in the IGPs, the magnetization of the IGPs in the Cu0.5 magnet is considered much lower compared to that in the Cu0 magnet. Non-ferromagnetic IGPs not only contribute to a large coercivity at room temperature, but also lead to a better thermal stability of coercivity as revealed by micromagnetic studies [30]. Therefore, the obtained stable β vs. T can be considered as another evidence for lower magnetization of the IGPs in the Cu0.5 magnet. The MOKE microscopy results (Fig. 5) show the stronger pinning effect of the domain walls at the grain boundaries in the Cu0.5 magnet compared to that of the Cu0 magnet, making the importance of the Fe-lean IGPs clearly visible. Therefore, the enhanced coercivity of the Cu0.5 magnet is due to the weakened inter-grain exchange-coupling of the $SmFe_{12}$-based phase, caused by the presence of Fe-lean IGPs. The improved microstructural parameter, α, of the Cu0.5 magnet compared to the Cu0 magnet (Fig. 1(d)), could be mainly attributed to the weakened exchange-coupling of the main phase grains. It should be noted that the contribution of the refined grain size to the coercivity can be effective only when the grains are exchange-decoupled. Therefore, the fine grain size and more importantly, the formation of Fe-lean IGP in this magnet led to the record-breaking coercivity value in the Cu0.5 magnet.

How to improve the extrinsic magnetic properties beyond the currently reported values in $SmFe_{12}$-based magnets remains an open question. Using the latest high-coercivity Nd–Fe–B magnet as the model, the pathway to an achievable microstructure and coercivity can be drawn for the $SmFe_{12}$ magnets. Fig. 6 presents the areal fraction of the constituent phases in the Cu0.5 $SmFe_{12}$-based magnet of this study ($\mu_0 H_c$ = 1.4 T, H_c/H_A = 0.14) compared with that of a high-coercivity Nd–Fe–B magnet ($\mu_0 H_c$ = 1.8 T, H_c/H_A = 0.26) [29]. In the case of the Cu0.5 magnet, the fraction of the rare-earth-oxide phase (SmO) is higher (6.8%) compared to that of the Nd–Fe–B magnet (NdO_x ~ 1.5%). This oxide phase deteriorates the continuity of the IGPs [32]. Therefore, the processing requires further optimization to control the oxidation of the $SmFe_{12}$-based alloy powder. Further, in the Nd–Fe–B magnet, the fraction of the desirable rare-earth-rich phases was higher (9.9%), which resulted in a typically 10 nm thick non-ferromagnetic IGP. This indicates that an increase in the fraction of the rare-earth-rich (Sm+SmCu)-based phase might lead to better continuity of thicker non-ferromagnetic IGPs enveloping all the $SmFe_{12}$ phase grains, resulting in even higher coercivity values. Moreover, a further decrease of the grain size towards the single domain size 0.6-0.75 μm [23] while maintaining the Fe-lean IGPs can also be exploited as another approach for coercivity enhancement. Overall, this demonstrates the potential of the $SmFe_{12}$-based magnet to exhibit a higher coercivity (up to or above 25% H_A) through microstructure engineering, including grain boundary engineering and grain refinement. As for the remanence enhancement, composition and process optimizations are required to eliminate the undesired SmO-, $SmFe_2$-, Fe_2Ti- and Ti-based phases, as well as to reduce the stabilizer content in the main phase, as these dilute the magnetization. Ultra low oxygen environment control in the sintering instruments could help in the reduction of the SmO phase. Overall, this comparison gives a guideline on how to further improve the magnetic properties of $SmFe_{12}$-based sintered magnets toward their practical application.

From the perspective of practical applications, the hard-magnetic properties of the Cu0.5 sintered magnet compared with other PM systems are shown in the remanence versus coercivity benchmark diagram, Fig. 7. It is seen that the coercivity reported in this work is the highest for $SmFe_{12}$-based magnets, and the M_r and H_c are comparable to those of isotropic Nd–Fe–B bonded magnets. Given the low cost of $SmFe_{12}$-based magnets, these can be considered as an alternative candidate for applications that use bonded Nd-Fe-B magnets but require a good thermal stability [33–36]. However, for practical applications as high-performance permanent magnets, an improvement of the M_r is necessary. It is to be noted that the $SmFe_{12}$ sintered magnets are mostly successfully prepared only with large amounts of stabilizers (Ti and V). Future studies need to be carried out on how to minimize these stabilizers to achieve higher M_r while maintaining the H_c values.

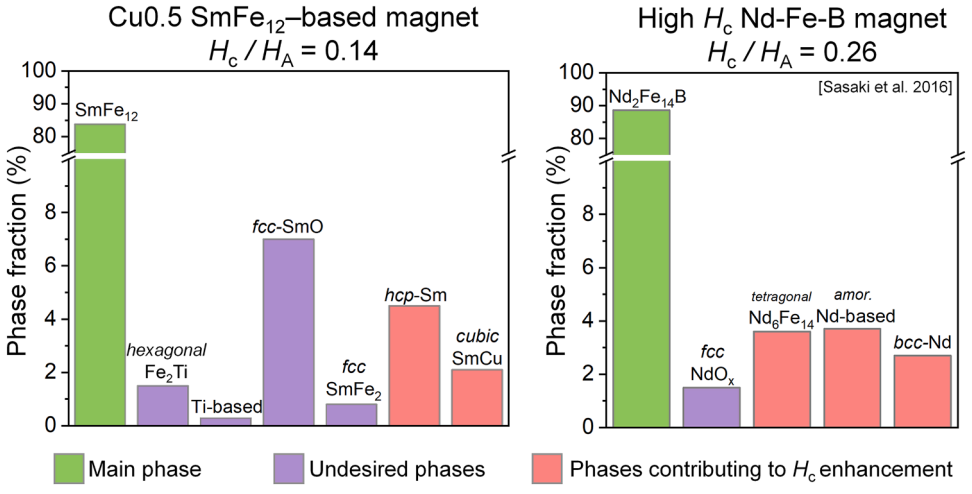

Fig. 6. Areal fraction of constituent phases in the Cu0.5 sintered magnet and a high-coercivity Nd-Fe-B sintered magnet [29].

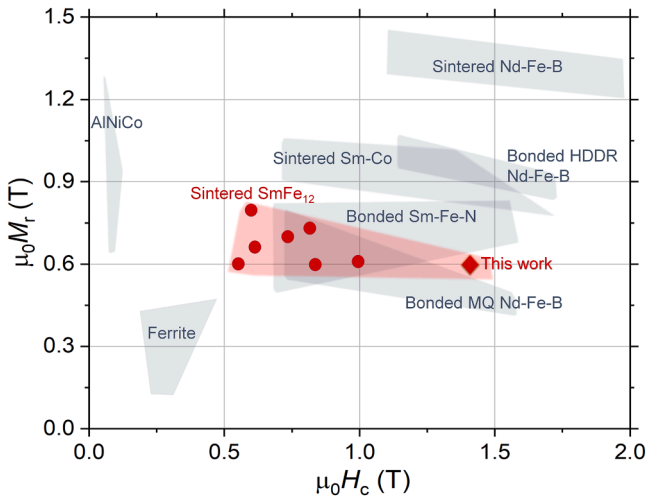

Fig. 7. Remanence versus coercivity benchmark diagram for bulk permanent magnets [22–24,33–36].

5. Conclusions

In this work, we optimized the processing route and alloy composition to achieve a high coercivity of 1.4 T in $SmFe_{12}$-based $ThMn_{12}$-type anisotropic sintered magnet. The general microstructure study revealed that the microalloying with Cu in combination with the use of strip-cast alloy as the starting materials leads to the formation of Fe-lean IGPs enveloping the $SmFe_{12}$ grains, which suppresses the exchange-coupling of the main phase grains and contributes to the record-breaking coercivity. This was experimentally confirmed by observing magnetization reversal using MOKE microscopy, wherein the reversed domain propagation is hindered in the Cu0.5 magnet owing to its weak intergranular exchange interaction. The role of Cu was revealed using TEM, wherein it led to the co-existence of the desirable Mg-type Sm-based and CsCl-type SmCu-based phases in the intergranular network, forming the Fe-lean (Sm+SmCu) eutectic. The Fe-lean intergranular phase not only improved the coercivity but also the thermal stability of coercivity. Overall, this work provides new insights on the microstructure dependency of coercivity in $SmFe_{12}$-based sintered magnets and discusses the future direction for the development of high-performance industrially viable $SmFe_{12}$-based magnets.

Declaration of Competing Interest

The authors declare that they have no known competing financial interests or personal relationships that could have appeared to influence the work reported in this paper.

Acknowledgments

This work was in-part supported by JSPS KAKENHI Grant Number JP23H01674, and MEXT Program: Data Creation and Utilization-Type Material Research and Development Project (Digital Transformation Initiative Center for Magnetic Materials) Grant Number JPMXP1122715503. We acknowledge Mr. Y. Toyooka for technical support. Xin Tang acknowledges ICYS for the provision of ICYS fellowship. A. K. Srinithi acknowledges Dr. Yukiko Takahashi for facilitating measurements.

Supplementary materials

Supplementary material associated with this article can be found, in the online version, at doi:10.1016/j.actamat.2023.119111.

References

[1] https://www.marketsandmarkets.com/Market-Reports/permanent-magnet-market-806.html.
[2] https://www.marketsandmarkets.com/Market-Reports/permanent-magnet-motor-market-218887711.html.
[3] https://www.virta.global/en/global-electric-vehicle-market.
[4] https://www.transparencymarketresearch.com/permanent-magnet-generators-market.html.
[5] R. W. McCallum, L. H. Lewis, R. Skomski, M. J. Kramer, and I. E. Anderson, Practical Aspects of Modern and Future Permanent Magnets Annual Review of Materials Research, 44 (2014), pp. 451–477, 10.1146/annurev-matsci-070813-113457.
[6] J. M. D. Coey, Perspective and Prospects for Rare Earth Permanent Magnets Engineering, 6 (2020), pp. 119–131, 10.1016/j.eng.2018.11.034.
[7] K. Ohashi, Y. Tawara, R. Osugi, M. Shimao, Magnetic properties of Fe-rich rare-earth intermetallic compounds with a ThMn12 structure, J. Appl. Phys. 64 (2018) 5714–5716, https://doi.org/10.1063/1.342235.
[8] S.F. Cheng, V.K. Sinha, Y. Xu, J.M. Elbicki, E.B. Boltich, W.E. Wallace, S.G. Sankar, D.E. Laughlin, Magnetic and structural properties of SmTiFe11-xCox alloys, J. Magn. Magn. Mater. 75 (1988) 330–338, https://doi.org/10.1016/0304-8853(88)90039-X.
[9] A.M. Gabay, G.C. Hadjipanayis, Recent developments in RFe12-type compounds for permanent magnets, Scripta Mater. 154 (2018) 284–288, https://doi.org/10.1016/j.scriptamat.2017.10.033.
[10] Y. Hirayama, Y.K. Takahashi, S. Hirosawa, K. Hono, Intrinsic hard magnetic properties of $Sm(Fe_{1-x}Co_x)_{12}$ compound with the ThMn12 structure, Scripta Mater. 138 (2017), https://doi.org/10.1016/j.scriptamat.2017.05.029.
[11] P. Tozman, H. Sepehri-Amin, K. Hono, Prospects for the development of SmFe12-based permanent magnets with a ThMn12-type phase, Scripta Mater. 194 (2021), 113686, https://doi.org/10.1016/j.scriptamat.2020.113686.
[12] D. Goll, S.Parkin Kronmuller, Micromagnetism-microstructure relations and the hysteresis loop, in: Handbook of Magnetism and Advanced Magnetic Materials, 2, Wiley, New York, NY, USA, 2007, pp. 1–36, https://doi.org/10.1002/9780470022184.hmm214.
[13] K. Hono, H. Sepehri-Amin, Strategy for high-coercivity Nd–Fe–B magnets, Scripta Mater. 67 (2012) 530–535, https://doi.org/10.1016/j.scriptamat.2012.06.038.
[14] A.M. Gabay, G.C. Hadjipanayis, High-coercivity ThMn12-type monocrystalline Sm–Zr–Fe–Co–Ti particles by high-temperature reduction diffusion, Scripta Mater. 196 (2021), 113760, https://doi.org/10.1016/j.scriptamat.2021.113760.
[15] D. Palanisamy, S. Ener, M. Maccari, L. Schäfer, K.P. Skokov, O. Gutfleisch, D. Raabe, B. Gault, Grain boundary segregation, phase formation, and their influence on the coercivity of rapidly solidified SmFe11Ti hard magnetic alloys, Phys. Rev. Mater. 4 (2020), 054404, https://doi.org/10.1103/PhysRevMaterials.4.054404.
[16] C. Zhu, Z. Liu, X. Fan, X. Gao, Z. Liu, W. Cheng, Z. Jia, R. Chen, A. Yan, X. Liu, Phase evolution of ThMn12-type Sm-Fe-Co-Ga-Ti alloys with annealing treatment, J. Alloys. Comp. 932 (2023), 167604, https://doi.org/10.1016/j.jallcom.2022.167604.
[17] I. Dirba, H. Sepehri-Amin, I.J. Choi, J.H. Choi, H.S. Uh, T.H. Kim, S.J. Kwon, T. Ohkubo, K, Hono SmFe12-based hard magnetic alloys prepared by reduction-diffusion process, J. Alloys. Comp. 861 (2021), 157993, https://doi.org/10.1016/j.jallcom.2020.157993.
[18] L. Zhao, C. Li, X. Zhang, S. Bandaru, K. Su, X. Liu, Q. Zhou, L. Li, J.M. Greneche, J. Jin, M. Yan, Effects of Sm content on the phase structure, microstructure and magnetic properties of the SmxZr0.2(Fe0·8Co0.2)11.5Ti0.5 (x=0.8–1.4) alloys, J. Alloys. Comp. 828 (2020), 154428, https://doi.org/10.1016/j.jallcom.2020.154428.
[19] I. Dirba, H. Sepehri-Amin, T. Ohkubo, K. Hono, Development of ultra-fine grain sized SmFe12-based powders using hydrogenation disproportionation desorption recombination process, Acta Mater. 165 (2019) 373–380, https://doi.org/10.1016/j.actamat.2018.11.065.
[20] T. Saito, F. Watanabe, D. Nishio-Hamane, Magnetic properties of SmFe12-based magnets produced by spark plasma sintering method, J. Alloys. Comp. 773 (2019) 1018–1022, https://doi.org/10.1016/j.jallcom.2018.09.297.
[21] X. Tang, J. Li, A.K. Srinithi, H. Sepehri-Amin, T. Ohkubo, K. Hono, Role of V on the coercivity of SmFe12-based melt-spun ribbons revealed by machine learning and microstructure characterizations, Scripta Mater. 200 (2021), 113925, https://doi.org/10.1016/j.scriptamat.2021.113925.
[22] K. Otsuka, M. Kamata, T. Nomura, H. Iida, H. Nakamura, Coercivities of Sm–Fe–M Sintered Magnets with $ThMn_{12}$-Type Structure (M = Ti, V), Mater. Trans. 62 (2021) 887–891, https://doi.org/10.2320/matertrans.MT-MBW2020003.
[23] J.S. Zhang, X. Tang, H. Sepehri-Amin, A.K. Srinithi, T. Ohkubo, K. Hono, Origin of coercivity in an anisotropic Sm(Fe,Ti,V)12-based sintered magnet, Acta Mater. 217 (2021), 117161, https://doi.org/10.1016/j.actamat.2021.117161.
[24] J.S. Zhang, X. Tang, A. Bolyachkin, A.K. Srinithi, T. Ohkubo, H. Sepehri-Amin, K. Hono, Microstructure and extrinsic magnetic properties of anisotropic Sm(Fe,Ti,V)12-based sintered magnets, Acta Mater. 238 (2022), 118228, https://doi.org/10.1016/j.actamat.2022.118228.
[25] W. Pei, C. He, F. Lian, G. Zhou, H. Yang, Structures and magnetic properties of sintered Nd–Fe–B magnets produced by strip casting technique, J. Magn. Magn. Mater. 239 (2002) 475–478, https://doi.org/10.1016/S0304-8853(01)00654-0.
[26] A.M. Schönhöbel, R. Madugundo, A.M. Gabay. J. M. Barandiaran, G. C. Hadjipanayis, Nanocrystalline Sm-based 1:12 magnets, Acta Materialia 200 (2020) 652–658, https://doi.org/10.1016/j.actamat.2020.08.075.

[27] D. Ogawa, X.D. Xu, Y.K. Takahashi, T. Ohkubo, S. Hirosawa, K. Hono, Emergence of coercivity in Sm(Fe0.8Co0.2)12 thin films via eutectic alloy grain boundary infiltration, Scripta Mater. 164 (2019) 140–144, https://doi.org/10.1016/j.scriptamat.2019.02.001.
[28] J. Li, X. Tang, H. Sepehri-Amin, T.T. Sasaki, T. Ohkubo, K. Hono, Angular dependence and thermal stability of coercivity of Nd-rich Ga-doped Nd–Fe–B sintered magnet, Acta Mater. 187 (2020) 66–72, https://doi.org/10.1016/j.actamat.2020.01.035.
[29] T.T. Sasaki, T. Ohkubo, Y. Takeda, T. Sato, A. Kato, Y. Kaneko, K, Hono Formation of non-ferromagnetic grain boundary phase in a Ga-doped Nd-rich Nd–Fe–B sintered magnet, Scripta Mater. 113 (2016) 218–221, https://doi.org/10.1016/j.scriptamat.2015.10.042.
[30] J. Li, X. Tang, H. Sepehri-Amin, T. Ohkubo, K. Hioki, A. Hattori, K. Hono, On the temperature-dependent coercivities of anisotropic Nd-Fe-B magnet, Acta Mater. 199 (2020) 288–296, https://doi.org/10.1016/j.actamat.2020.08.040.
[31] H. Kronmüller, K.-D. Durst, M, Sagawa Analysis of the magnetic hardening mechanism in RE-FeB permanent magnets, J. Magn. Magn. Mater. 74 (1988) 291–302, https://doi.org/10.1016/0304-8853(88)90202-8.
[32] W.F. Li, T. Ohkubo, K. Hono, M. Sagawa, The origin of coercivity decrease in fine grained Nd–Fe–B sintered magnets, J. Magn. Magn. Mater. 321 (2009) 1100–1105, https://doi.org/10.1016/j.jmmm.2008.10.032.
[33] https://mqitechnology.com/applications/automotive/.
[34] https://product.tdk.com/en/products/magnet/index.html.
[35] http://www.umag.com.cn/index.php?m=&c=Index&a=lists&catid=2.
[36] K. Binnemans, P.T. Jones, T. Müller, L. Yurramendi, Rare, earths and the balance problem: how to deal with changing markets, J. Sustain. Metall. 4 (2018) 126–146, https://doi.org/10.1007/s40831-018-0162-8.